energy&fuels

pubs.acs.org/EF Article

Spraying Model PAHs on a Charged TiO_2 Surface for High-Efficiency Degradation

Jana L. van den Berg, Yin-Hung Lai, Garrett A. Wadsworth, William A. Lamberti, Hyung Woo, Sumathy Raman, and Richard N. Zare*

Cite This: *Energy Fuels* 2020, 34, 4289–4295 Read Online

ACCESS | Metrics & More | Article Recommendations | Supporting Information

ABSTRACT: The degradation of four model PAH compounds was studied by spraying from a micrometer-sized, grounded nozzle a solution of the PAH in a 1:1 solvent of toluene and isopropanol with a trace of water onto wetted TiO_2 anatase nanoparticles, which were immobilized on an etched stainless-steel support charged at +2 kV. Rubrene was chosen because of its established degradation pathways, and 1-methylpyrene, 2-methylnapththalene, and bis(pyren-1-yl)ethane were chosen because of their molecular structure, containing aromatic islands with short aliphatic groups, representative of a thermally and catalytically processed heavy feed stream. The fractional reaction yield was measured using different support materials and by applying different external voltages to the metal substrate. The optimized method yielding 75% degradation was applied to the other three PAHs, resulting in higher-mass degradation products, apparently formed via radical polymerization.

INTRODUCTION

In the refining of petroleum, much interest exists in how to convert low-value heavy components to lighter compounds that have higher value owing to their increased petrochemical utility.[1−3] The heavy oil fractions of the crude oil can be upgraded by a number of processes, which are often limited by the high viscosity of the material, mostly owing to the asphaltene content.[4−10] Chemically, asphaltenes consist of multiring aromatic cores that are linked together, either with alkyl groups of varying length or directly, for example, with strong biaryl C−C bonds[11] (e.g., C−C bond dissociation energy in biphenyl is ∼114 kcal/mol, see Figure 1a). They dissolve in an aromatic solvent but not in a paraffinic solvent and have high boiling points, often requiring solvents and catalysts at high temperatures for their upgrading.[5,9]

Recently, Lai et al.[12] presented a new approach to upgrade asphaltenes, developed on the example of the polycyclic aromatic hydrocarbon (PAH) rubrene (Figure 1b), i.e., by dissolving the compounds in a solvent and spraying them from a micrometer-sized capillary with a sheath gas. Subsequently, the microdroplets (MD) formed in the spray hit the wetted surface of anatase-phase titanium dioxide nanoparticles (TiO_2 NP), charged at +2 kV. The *in situ* formed hydroxyl radicals (OH·) initiate the degradation, resulting in a total degradation fraction of about 15% for rubrene. By repeating this treatment, the degradation increases to over 20% after the second treatment and up to 35% after the third. It is proposed that the degradation is limited by the surface density of TiO_2, the applied voltage, and the droplet size.[12]

The formation of the OH· radicals takes place in the charged TiO_2 NPs. The mechanistic understanding of the hole-induced oxidation of water is well established and explored in more detail elsewhere.[13,14] In short, the applied voltage generates an electron−hole pair, where the hole can oxidize other species on the NP surface.[14,15] In the presence of water, the holes oxidize the water to form highly reactive OH· radicals, which have been found to degrade aromatic systems. Addition of an OH·

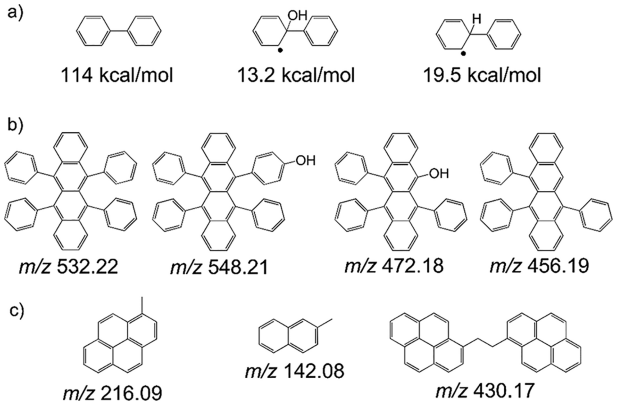

Figure 1. (a) Biaryl C−C bond energies of biphenyl, the hydroxylated biphenyl radical, and the hydrogenated radical (B3LYP/6-31G*). (b) Molecular structures of rubrene (*m*/*z* 532.22) and degradation products (*m*/*z* 548.21, *m*/*z* 472.18, and *m*/*z* 456.19). Rubrene degradation can occur via OH· addition, OH· substitution of a side ring, or removal of a side ring by the OH·. (b) Molecular structures of validation molecules 1-methylpyrene (1MP, *m*/*z* 216.09), 2-methylnaphthalene (2MN, *m*/*z* 142.08), and bis(pyren-1-yl)ethane (BPE, *m*/*z* 430.17).

Received: January 6, 2020
Revised: March 8, 2020
Published: March 12, 2020

https://dx.doi.org/10.1021/acs.energyfuels.0c00068
Energy Fuels 2020, 34, 4289−4295

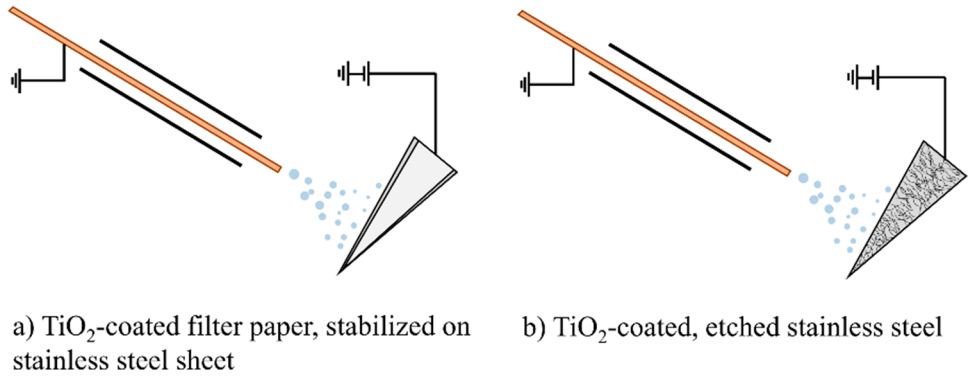

Figure 2. Spray setup with (a) filter paper and (b) etched stainless steel. The filter paper is stabilized by a stainless steel sheet to prevent bending by the sheath gas.

radical to biaryls weakens the aryl−aryl bond; B3LYP/6-31G* calculations show that the C−C bond energy in a hydroxylated biphenyl radical is more than 5 kcal/mol lower than that in a hydrogenated biphenyl radical (Figure 1a). For rubrene, OH· can add on to the aromatic rings or replace the aromatic side rings on the aromatic body, as shown in Figure 1b. In combination with the applied voltage, the TiO_2 NP coverage of the support surface is expected to be the limiting factor because more polycyclic aromatic hydrocarbons (PAHs) can react if a larger number of OH· radicals are supplied.

In the OH· radical formation route described above, the OH· radicals are formed on the surface of the TiO_2 nanoparticles. In addition, there is another way to form OH· radicals which is relevant for this work; it was shown recently that OH· can be formed from water in MD.[16] In many known cases it was found that reactions are accelerated[17−22] or enabled[16,17,23] in MD. For example, if water alone is sprayed in a setup as described above, spontaneous formation of hydrogen peroxide from recombination of OH· was observed.[16] The postulated reaction mechanism for the OH· on the MD surface involves the strong electric field on the order of 10^9 V/m at the air−water interface, causing the oxidation of OH^-. This ion exists in water-containing MD as the water's autoionization into H^+ and OH^- is strongly enhanced on the water droplet surface.[24] In general, it was found that smaller droplets, for example, generated by a higher sheath gas pressure, a smaller spray capillary, or a quickly evaporating solvent, lead to higher reaction acceleration.[16,22] Therefore, a higher fractional reaction yield (FRY) may be expected with smaller droplet sizes, if water is present in the spray solvent.

This work seeks to increase the degradation efficiency for the approach presented and to understand the underlying degradation mechanisms in more detail. The first objective is to find a way to increase the degradation yield so that the degradation arising from the two different OH· radical sources can be characterized in more detail, in particular, in terms of the voltage requirement for degradation onset. One way to achieve a higher degradation yield is presented. The support for the TiO_2 NPs is improved by (1) stabilizing the previously used filter paper with the immobilized TiO_2 NPs with a stainless-steel back rest against the spraying pressure, (2) refreshing the water supply on the TiO_2 NPs regularly during the experiment to ensure a constant water abundance and prevent it from drying out, (3) employing a movable spray head to use a larger TiO_2 area, and most importantly, (4) replacing the previously used support material (filter paper) with an etched stainless steel plate. As a second objective, the degradation strategy is extended to model compounds that can probe reaction pathways. Good candidates are 1-methylpyrene (1MP), 2-methylnaphthalene (2MN), and bis(pyren-1-yl)-ethane (BPE) as they consist of aromatic bodies and aliphatic parts, as shown by the molecular structures in Figure 1c.

MATERIALS AND METHODS

Support Preparation. Filter paper (Fisherbrand Filter Paper, P4, medium-to-fine porosity) was cut into triangular pieces (approximately 1 cm × 2.5 cm × 2.5 cm edge lengths) and sonicated in an aqueous 2.5 mg/mL suspension of TiO_2 NPs (anatase, 25 nm diameter, CAS 1317-70-0, Sigma-Aldrich, sonicated for 30 min) for 2 min. They were fastened in the high-voltage connector clamp together (Figure 2a) with a similarly sized stainless steel plate (thickness: 0.2 mm).

Stainless steel plates were cut into small triangular pieces (approximately 1 cm × 2.5 cm × 2.5 cm edge lengths) and cleaned in methanol by 15 min sonication. For the etching process, similar to Rao et al.,[25] the pieces were dried off and treated with concentrated hydrochloric acid (37.5%, CAS 7647-01-0, Sigma-Aldrich) for 72 h. After the acid was rinsed off with sufficient water, the pieces were sonicated in an aqueous 2.5 mg/mL suspension of TiO_2 NPs (sonicated for 30 min) or in an aqueous bulk-TiO_2 (anatase, powder, 99.8%, Sigma-Aldrich, CAS 1317-70-0) solution of the same concentration for 2 min before calcining at 250 °C overnight. In order to apply multiple coating layers, the sonication and calcining steps were repeated. The coated stainless steel supports was directly fastened in the high-voltage connector clamp (Figure 2b).

The sample surface morphologies were studied with a scanning electron microscope (SEM) using a Zeiss CrossBeam540 at the ExxonMobil Research and Engineering Company's Corporate Strategic Research Laboratory in Annandale, New Jersey. Instrumental conditions were as follows: 3−7 kV accelerating voltage with a 6 nm Cr-metal coating for enhanced conductivity. A range of imaging conditions and detector combinations (SE, SE2, and BEI) were employed in order to permit evaluation of the surface structures at various length scales and surface sensitivities.

Degradation Procedure. 1MP (CAS 2381-21-7, Frontier Scientific), 2MN (CAS 91-57-6, Sigma-Aldrich), BPE (Tyger Scientific), and rubrene (CAS 517-51-1, Sigma-Aldrich) were dissolved in a 1:1 volumetric mixture of isopropanol and toluene (IP/T) at a concentration of 0.02 mg/mL, unless otherwise noted, and sprayed from a fused-silica capillary (flexible, with polyimide coating, Molex, LLC, inner diameter 100 μm, outer diameter 300 μm) with a syringe pump (pump rate 25 μL/min, Harvard Apparatus Infusion) and compressed air (Praxair, sheath gas pressure 60 psi) from a concentric steel tube around the capillary (diameter 1.7 mm).

The spray source was kept at a distance of 2.5 cm from the support with the charged TiO_2 NPs (Keithley 247 high-voltage supply), as depicted in Figure 2. The position of the spray on the TiO_2 NP was

https://dx.doi.org/10.1021/acs.energyfuels.0c00068
Energy Fuels 2020, 34, 4289−4295

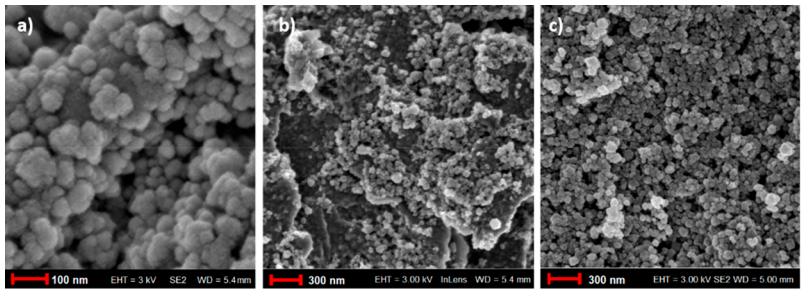

Figure 3. SEM images of TiO_2 on (a) filter paper, (b) etched stainless steel with one layer of coating, and (c) stainless steel with three layers of coating.

changed with an *xyz*-translational stage, so that the whole coated area was used. The syringe needle was grounded and the current against ground at the spray tip was monitored with a picoammeter (Keithley 485 autoranging picoammeter) to verify that no significant current was flowing (<30 pA, as expected for sonic sprays[26]). After every 100 μL sprayed, the power supply was turned off, and 1−2 drops of water were added onto the TiO_2 NPs.

Analysis with Laser Desorption Laser Ionization Mass Spectrometry. The TiO_2NPs were washed ten times with 100 μL of the solvent used. The rinsate was dropcast onto a glass platter, which was fastened onto a metal sample holder. The laser desorption laser ionization mass spectrometer (L^2MS) is in detail described elsewhere.[12,27] Briefly, the sample is introduced into a high vacuum (10^{-8} Torr) and evaporated with a CO_2 laser beam (wavelength 10.6 μm, Alltech AL 882 APS) before the isolated molecules in the neutral plume are ionized with a laser pulse from the ionization laser (Coherent, ExciStar XS 157 nm, EXS-2000XS-L). The produced ions are extracted by and accelerated away from the ionization region by voltage plates kept between 2.5 kV and 2.1 kV. The detection efficiency is dependent on the mass and ionization cross section but is on the same order of magnitude for the parent ions and the degradation products.[27] Hence, the FRY is reported as the ratio of the peak height of the product to the sum of all peak heights. The use of FRY is a reasonable practical compromise also employed in previous work,[12] which assumes we detect all species that represent the sample composition using the approach herein. After passing through the Wiley−McLaren time-of-flight tube, the ions strike a multichannel plate detector system charged at −2 kV (Chevron configuration, Photonis USA, 25 mm active area), releasing an electrical current that is collected at an anode, amplified (amplification: 2× coarse gain, 2× fine gain, 20 ns integration time, Ortec 474 timing filter amplifier) and observed with an oscilloscope (LeCroy Waverunner LT342). Every mass spectrum represents an average of 50 laser shot pairs, and 3−10 spots on the analyte surface are sampled. The recorded time-of-flight data is converted to m/z spectra with a calibration curve using three aromatic molecules of known mass spanning the range m/z 202−619.

RESULTS AND DISCUSSION

Rubrene Degradation on Different TiO_2 NP Supports. Rubrene was treated with the method described above on three different TiO_2 NP support types, i.e., on a modified filter paper support, on a single-coated stainless-steel support, and on a triple-coated stainless-steel support. The advantage of filter paper was the large surface area, arising from the three-dimensional cellulose fiber structure as can be seen in the SEM image in Figure 3a. However, there were two major drawbacks, namely, cellulose's lack of conductivity significantly lowers the electric field strength for the given applied potential, and it does not withstand higher temperatures that can immobilize the TiO_2 NPs permanently through a calcining process. Both drawbacks could be mitigated by replacing the filter paper material with stainless steel except that the surface area of stainless steel is significantly smaller than that of filter paper. In order to increase the surface area, an etching step was introduced. Figure 3b shows a single-coated support where the roughened surface is barely covered with a monolayer of TiO_2 NPs. Figure 3c shows an SEM image of the triple-coated support. It is seen that after three coating processes, a thick NP layer has formed on the surface, completely covering the roughened features. This layer was stable for the whole study period of six months. No decline in catalytic performance was found, nor was any change in surface morphology detected.

The degradation product peaks obtained for the three support types are summarized in Table S1, and a sample mass spectrum is presented in Figure 4. All support models were

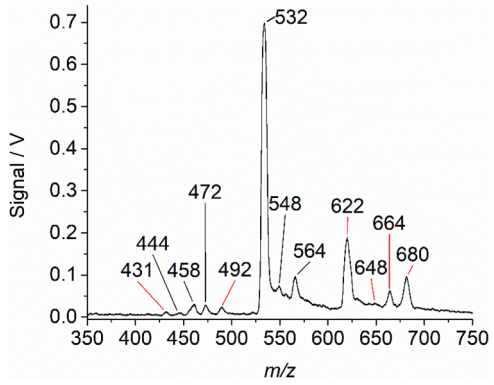

Figure 4. Representative mass spectrum for rubrene degradation on the triple-coated stainless-steel support showing the parent ion (m/z 532) with already known peaks marked in black and newly detected peaks in red. This spectrum was taken for one of the samples, so that not all product peaks listed in Table S1 show with the same clarity.

tested in triplicate. Figure 4 shows one representative mass spectrum obtained for a degradation sample with triple-coated TiO_2 support; most of the peaks listed in Table S1 can be clearly seen, but some peaks appear more strongly in other spectra. As possible degradation pathways for rubrene have been studied before with this degradation approach, a number of product peaks could be assigned, which are labeled in black in Figure 4, including the parent ion peak. This improved method was able to observe more products than previously reported, and new peaks in the product mass spectrum are marked in red.

The FRY was calculated from the sum of the product peak heights divided by the sum of the peak heights of all peaks observed, including the rubrene parent peak. Figure 5 shows the FRY measured for the different support models, where the FRY measured for the known product peaks is represented in black. The FRY taking into account all product peaks,

https://dx.doi.org/10.1021/acs.energyfuels.0c00068
Energy Fuels 2020, 34, 4289−4295

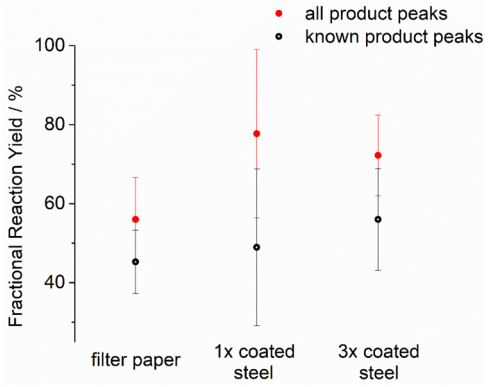

Figure 5. FRY calculated from peak height ratios taking into account the known product peaks (black) and all product peaks (red). Both coated stainless-steel supports produced higher FRY, probably because the higher conductivity compensated for the lower surface coverage. The error bars represent the standard deviation between three samples, respectively.

including the newly observed products peaks, are represented in red. The stainless-steel support increased the FRY, indicating that the higher conductivity probably compensated for the lower surface area. The two coated stainless-steel supports did not show significantly different reaction yields, indicating that the conductivity of the material, and hence the electric field strength, plays a more important role than the surface coverage. This was confirmed by a simple test; after the effective voltage at the TiO_2 support was measured with a multimeter, it became clear that the filter paper material suffered a substantial voltage reduction after drying out, effectively becoming an electric insulator. The electric field emanating from the conducting support could still continue to exert a force on the incoming microdroplets, polarize the droplets, align the molecules, and ionize droplets, however to a lesser extent due to the decreased electric field strength. For the stainless-steel supports, and the thoroughly wetted filter paper support, the effective voltage on the TiO_2 NPs was measured to be the applied voltage. However, exposure to the sheath gas dried out the surface of the filter paper support after a few minutes, resulting in an effective voltage of 100 V instead of 2 kV only millimeters away from the electrode. At the opposite end of the dry filter paper, which then acted as a resistor, only 15 V remained. Therefore, the stainless steel support presented a sturdier system and was chosen for further characterization.

Control Experiments for Rubrene Degradation. As described above, the degradation reaction needs OH· radicals to proceed. These radicals can either be formed from dissolved water in the MD or by charging wet TiO_2 NP. To examine the contributions from either OH· radical source, control experiments selectively disabled one or both of the sources. These experiments were all carried out using the triple-coated stainless-steel support as this yielded better reproducibility as indicated in Figure 5.

In order to investigate the impact of the wet TiO_2 NPs on the degradation, the TiO_2 activity was inhibited (a) by not supplying water to the TiO_2 NPs, or (b) by not applying voltage to generate the electron−hole pair, or (c) by replacing the TiO_2 NP coating with a TiO_2 bulk coating. The result was a significantly lower FRY in all three cases. To learn more about the effect of the MD on the degradation, the reaction solution was (d) directly deposited onto the TiO_2 NP support without spraying it, and (e) the experiment was repeated in toluene, a solvent that did not contain OH groups but was likely to form OH· radicals from dissolved water. One additional control experiment (f) combined all previously mentioned controls into one, i.e., a rubrene solution in toluene was deposited as bulk solution onto a dry stainless steel support that was coated with bulk TiO_2 without applying a charge.

Figure 6 shows the result for all tests relative to the starting material rubrene; only about a third of the degradation product

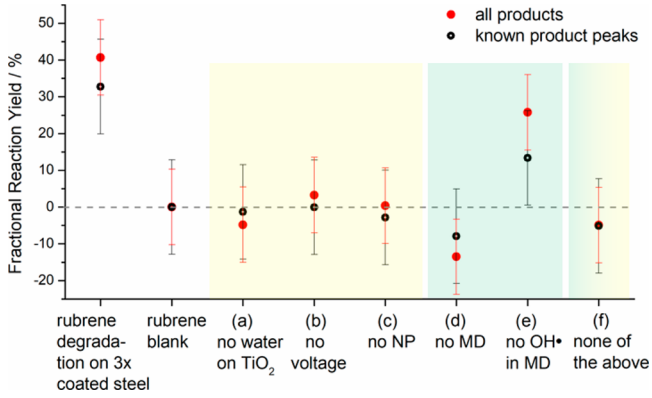

Figure 6. Summary of the FRY for the regular treatment process on the triple-coated stainless steel support, for processes without activated TiO_2 NPs (shaded in yellow) and for processes without OH•radicals from the MD source (shaded in green), taking into account the known product peaks (black circles) and all product peaks (red dots), all referenced to the rubrene blank. The last control experiment combined all others in one (shaded in yellow and green). All control experiments (a−f) show significantly less efficiency, on the order of magnitude of a rubrene sample by itself. Only by using the complete degradation procedure can the high efficiency be obtained. The error bars represent the standard deviation of three degradation samples (left), giving an impression of variation for the control experiments (a−f).

formation was detected when no OH· radicals could be formed via the described routes in either the MD or the TiO_2 NPs. As a result, the high degradation efficiencies could only be obtained if the reaction took place with OH-containing MD on wetted and charged TiO_2 NPs.

Dependence of Rubrene Degradation on Applied Voltage. In order to characterize the reaction properties further, the complete degradation experiment was carried out with different voltages, i.e., different electric fields on the TiO_2 NP. Again, all experiments were carried out using the triple-coated stainless-steel support as it yielded the highest reproducible degradation efficiency. Figure 7 shows that at voltages as low as 1 kV, about the same amount of products was formed as for the control experiments (Figure 6). At 1.5 kV, there was more product formation; however, not as much as in the reactions presented in the first part of this work. This indicates that the onset voltage for OH· generation is between 1 kV and 1.5 kV, and there is a gradual increase above those voltages. More OH· radicals seem to be generated when a higher voltage is supplied to the wet TiO_2.

1MP, 2MN, and BPE Degradation. By reacting more model compounds, this reaction approach was also tested to determine whether it was applicable to more PAHs than rubrene. The first candidates were 1MP, 2MN, and BPE

https://dx.doi.org/10.1021/acs.energyfuels.0c00068
Energy Fuels 2020, 34, 4289−4295

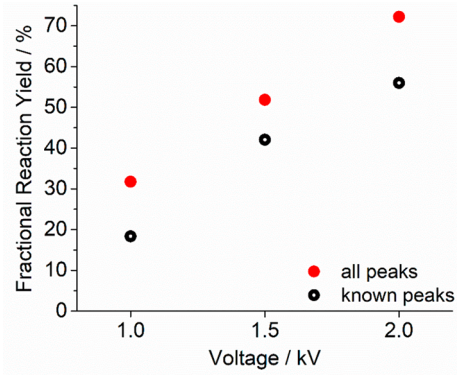

Figure 7. Trend for rubrene degradation on the triple-coated stainless-steel support at different voltages; the amount of product formed at 1 kV seems to be comparable to amount detected in the control experiments. For higher voltages applied, the OH· generation seems to gradually increase further.

(Figure 1c), naphthalene and pyrene derivatives with aliphatic side chain. The same parameters were used as for rubrene on the triple-coated stainless-steel support. In the mass spectra shown in Figures 8a–c, new peaks are mostly observed at higher masses than the parent peaks, suggesting that this process does not simply fragment the aromatic ring. Instead, it is speculated that the relatively stable benzylic radical formed from 1MP and/or 2MN undergoes a chemical change that leads to an increase in the molecular weight. These new peaks indicate that a reaction has occurred. By the virtue of the product m/z being higher than the reactant m/z, a polymerization of naphthalene substructures is possible, potentially initiated by the OH· radicals.

The efficiency of this process depends on the molecular architecture of the parent molecule in terms of alkyl side chain length, alkyl chain position on the aromatic body, and length of alkyl chain bridge in between the aromatic islands.

Similarly to 1MP, 1-dodecylpyrene (DDP) shows high-mass product peaks after treatment, with one fragment peak around m/z 207. This suggests that the OH· radical prefers to undergo a barrierless addition to the aromatic ring followed by scission of the benzylic C–C bond rather than abstracting a hydrogen from any carbon of the alkyl side chain, leading to a series of alkenylpyrene and light gas. This is observed to a smaller degree for DDP, as shown in Figure S1. It is possible that the long alkyl chain poses a steric hindrance to the addition to the aromatic ring. In addition, our current experimental setup does not collect any light gases that are formed from the fragmentation of dodecyl side chains.

In comparison to 2MN, the structural isomer 1-methylnaphthalene (1MN) does not undergo the reaction as readily (see Figure S2), which could be explained by different radical stabilities or by the fact that 1MN evaporates more quickly, thereby leaving less starting material to react. Additionally, the polymerization reaction in 1MN is possibly hindered by proximity to the ring fusion center as opposed to 2MN. In order to suppress the formation of products with higher molecular weight, we carried out additional experiments with a hydrogen donor, tetralin, so as to cap the radical with hydrogen. However, the barrier involved in H-abstraction from tetralin prevents it from occurring readily under ambient conditions, and the polymerization reaction is likely to occur very quickly, even when hydrogen donor molecules like tetralin were present. In addition, treatment of tetralin alone causes product formation with high molecular weight (Figure S3).

The degradation of BPE was compared to the degradation of bis(pyren-1-yl)methane (BPM), which has a shorter alkyl bridge in between the two pyrenyl substituents. No degradation was observed for BPM, suggesting a more stable reactant or transition-state radical (Figure S4).

CONCLUSIONS

The degradation approach for asphaltene degradation by OH· radicals was further developed on the rubrene model system, resulting in a 5-fold increase in efficiency in rubrene degradation and the detection of new products. This was achieved by identifying the crucial reaction parameters and optimizing the treatment process correspondingly. A conductive TiO_2 NP support was required to ensure the effective charge on the TiO_2 NPs, and sufficient water had to be supplied for OH· radical generation. The highest degradation efficiency (75%) was achieved with water-containing MD and charged and wetted TiO_2 NPs, where the spray head was constantly moved across the TiO_2 NP coating. The improved treatment was successfully tested by degrading other PAHs. The results of this study encourage the degradation of additional, different types of PAHs.

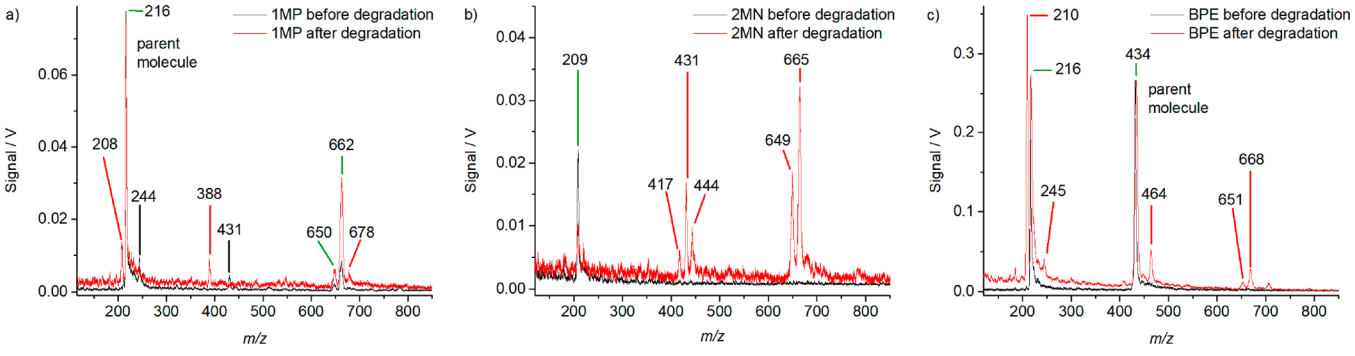

Figure 8. (a) 1MP, (b) 2MN, and (c) BPE spectra taken before (black) and after (red) treatment with the degradation method. (a) Parent molecule of 1MP at m/z 216 and products at m/z 208, m/z 388, and m/z 662. (b) 2MN product peaks m/z 431 and m/z 665. (c) Parent molecule of BPE at m/z 434 with product peaks at m/z 210, m/z 464, and around m/z 668. Peaks that predominantly show up in the original spectrum are marked in black, peaks from the processed sample in red, and peaks occurring in both spectra in green.

https://dx.doi.org/10.1021/acs.energyfuels.0c00068
Energy Fuels 2020, 34, 4289–4295

■ ASSOCIATED CONTENT

Supporting Information

The Supporting Information is available free of charge at https://pubs.acs.org/doi/10.1021/acs.energyfuels.0c00068.

Summary of observed product peaks after rubrene degradation and mass spectra of other PAHs (1-dodecylpyrene, 1-methylnaphthalene, 2-methylnaphthalene, and bis(pyren-1-yl)methane) with degradation products used to test the presented method (PDF)

■ AUTHOR INFORMATION

Corresponding Author

Richard N. Zare − *Department of Chemistry, Stanford University, Stanford, California 94305, United States;* orcid.org/0000-0001-5266-4253; Email: rnz@stanford.edu

Authors

Jana L. van den Berg − *Department of Chemistry, Stanford University, Stanford, California 94305, United States*

Yin-Hung Lai − *Department of Chemistry, Stanford University, Stanford, California 94305, United States; Department of Chemical Engineering, National United University, Miaoli, Taiwan 360, Republic of China*

Garrett A. Wadsworth − *ExxonMobil Research and Engineering, Annandale, New Jersey 08801, United States*

William A. Lamberti − *ExxonMobil Research and Engineering, Annandale, New Jersey 08801, United States*

Hyung Woo − *ExxonMobil Research and Engineering, Annandale, New Jersey 08801, United States*

Sumathy Raman − *ExxonMobil Research and Engineering, Annandale, New Jersey 08801, United States*

Complete contact information is available at: https://pubs.acs.org/10.1021/acs.energyfuels.0c00068

Author Contributions

The manuscript was written through contributions of all authors. All authors have given approval to the final version of the manuscript. The degradation procedure and analysis with mass spectrometry was carried out in the laboratories in Stanford University by Jana L. van den Berg. All SEM images were taken at the ExxonMobil site by Garrett A. Wadsworth and William A. Lamberti.

Funding

This work was funded by an ExxonMobil Research and Engineering grant, agreement no. EM11163.TO2 and SPO-135222.

Notes

The authors declare no competing financial interest.

■ ACKNOWLEDGMENTS

J.L.B. thanks ExxonMobil for an ExxonMobil Emerging Energy Research Fellowship.

■ NOMENCLATURE

1MN = 1-methylnaphthalene
1MP = 1-methylpyrene
2MN = 2-methylnaphthalene
BPE = bis(pyren-1-yl)ethane
BPM = bis(pyren-1-yl)methane
DDP = 1-dodecylpyrene
IP/T = 1:1 volumetric mix of isopropanol and toluene
m/z = mass-to-charge ratio
L^2MS = laser desorption laser ionization mass spectrometry
NP = nanoparticles
OH· = hydroxyl radicals
PAH = polycyclic aromatic hydrocarbons
SEM = scanning electron microscope
TiO_2 = titanium dioxide

■ REFERENCES

(1) Covert, T.; Greenstone, M.; Knittel, C. R. Will We Ever Stop Using Fossil Fuels? *Journal of Economic Perspectives* **2016**, *30* (1), 117−38.

(2) Greene, D. L.; Hopson, J. L.; Li, J. Have we run out of oil yet? Oil peaking analysis from an optimist's perspective. *Energy Policy* **2006**, *34* (5), 515−531.

(3) Tullo, A. H. Why the future of oil is in chemicals, not fuels. *Chem. Eng. News*; 2019; https://cen.acs.org/business/petrochemicals/future-oil-chemicals-fuels/97/i8.

(4) Chapter 1 - Refining Heavy Oil and Extra-heavy Oil. In *Heavy and Extra-heavy Oil Upgrading Technologies*; Speight, J. G., Ed.; Gulf Professional Publishing: Boston, 2013; pp 1−13.

(5) Chapter 2 - Thermal Cracking. In *Heavy and Extra-heavy Oil Upgrading Technologies*; Speight, J. G., Ed.; Gulf Professional Publishing: Boston, 2013; pp 15−38.

(6) Ilyin, S.; Arinina, M.; Polyakova, M.; Bondarenko, G.; Konstantinov, I.; Kulichikhin, V.; Malkin, A. Asphaltenes in heavy crude oil: Designation, precipitation, solutions, and effects on viscosity. *J. Pet. Sci. Eng.* **2016**, *147*, 211−217.

(7) Alawad, I.; Al Zubaidi, I. Advances in Upgrading Process of Petroleum Residue: A Review. *EJERS* **2019**, *4* (6), 104−110.

(8) Sahu, R.; Song, B. J.; Im, J. S.; Jeon, Y.-P.; Lee, C. W. A review of recent advances in catalytic hydrocracking of heavy residues. *J. Ind. Eng. Chem.* **2015**, *27*, 12−24.

(9) Yan, T.; Xu, J.; Wang, L.; Liu, Y.; Yang, C.; Fang, T. A review of upgrading heavy oils with supercritical fluids. *RSC Adv.* **2015**, *5* (92), 75129−75140.

(10) Chapter 10 - Refinery of the Future. In *The Refinery of the Future*; Speight, J. G., Ed.; William Andrew Publishing: Boston, 2011; pp 315−340.

(11) Zhu, J.; Wang, J.; Dong, G. Catalytic activation of unstrained C(aryl)-C(aryl) bonds in 2,2′-biphenols. *Nat. Chem.* **2019**, *11* (1), 45−51.

(12) Lai, Y.-H.; Zhou, Z.; Basheer, C.; Zare, R. N. Upgrading Asphaltenes by Oil Droplets Striking a Charged TiO_2-Immobilized Paper Surface. *Energy Fuels* **2017**, *31* (11), 12685−12690.

(13) Nosaka, Y.; Nosaka, A. Understanding Hydroxyl Radical (•OH) Generation Processes in Photocatalysis. *ACS Energy Letters* **2016**, *1* (2), 356−359.

(14) Schneider, J.; Matsuoka, M.; Takeuchi, M.; Zhang, J.; Horiuchi, Y.; Anpo, M.; Bahnemann, D. W. Understanding TiO_2 Photocatalysis: Mechanisms and Materials. *Chem. Rev.* **2014**, *114* (19), 9919−9986.

(15) Frank, S. N.; Bard, A. J. Heterogeneous photocatalytic oxidation of cyanide ion in aqueous solutions at titanium dioxide powder. *J. Am. Chem. Soc.* **1977**, *99* (1), 303−304.

(16) Lee, J. K.; Walker, K. L.; Han, H. S.; Kang, J.; Prinz, F. B.; Waymouth, R. M.; Nam, H. G.; Zare, R. N. Spontaneous generation of hydrogen peroxide from aqueous microdroplets. *Proc. Natl. Acad. Sci. U. S. A.* **2019**, *116*, 19294.

(17) Lee, J. K.; Samanta, D.; Nam, H. G.; Zare, R. N. Spontaneous formation of gold nanostructures in aqueous microdroplets. *Nat. Commun.* **2018**, *9* (1), 1562.

(18) Lee, J. K.; Kim, S.; Nam, H. G.; Zare, R. N. Microdroplet fusion mass spectrometry for fast reaction kinetics. *Proc. Natl. Acad. Sci. U. S. A.* **2015**, *112* (13), 3898.

(19) Jansson, E. T.; Lai, Y.-H.; Santiago, J. G.; Zare, R. N. Rapid Hydrogen-Deuterium Exchange in Liquid Droplets. *J. Am. Chem. Soc.* **2017**, *139* (20), 6851−6854.

(20) Girod, M.; Moyano, E.; Campbell, D. I.; Cooks, R. G. Accelerated bimolecular reactions in microdroplets studied by desorption electrospray ionization mass spectrometry. *Chem. Sci.* **2011**, *2* (3), 501−510.
(21) Yan, X.; Bain, R. M.; Cooks, R. G. Organic Reactions in Microdroplets: Reaction Acceleration Revealed by Mass Spectrometry. *Angew. Chem., Int. Ed.* **2016**, *55* (42), 12960−12972.
(22) Marsh, B. M.; Iyer, K.; Cooks, R. G. Reaction Acceleration in Electrospray Droplets: Size, Distance, and Surfactant Effects. *J. Am. Soc. Mass Spectrom.* **2019**, *30*, 2022.
(23) Yan, X.; Cheng, H.; Zare, R. N. Two-Phase Reactions in Microdroplets without the Use of Phase-Transfer Catalysts. *Angew. Chem., Int. Ed.* **2017**, *56* (13), 3562−3565.
(24) Bai, C.; Herzfeld, J. Surface Propensities of the Self-Ions of Water. *ACS Cent. Sci.* **2016**, *2* (4), 225−231.
(25) Nageswara Rao, P; Kunzru, D. Fabrication of microchannels on stainless steel by wet chemical etching. *J. Micromech. Microeng.* **2007**, *17* (12), N99.
(26) Hirabayashi, A.; Fernández de la Mora, J. Charged droplet formation in sonic spray. *Int. J. Mass Spectrom. Ion Processes* **1998**, *175* (3), 277−282.
(27) Wang, W.; Taylor, C.; Hu, H.; Humphries, K. L.; Jaini, A.; Kitimet, M.; Scott, T.; Stewart, Z.; Ulep, K. J.; Houck, S.; Luxon, A.; Zhang, B.; Miller, B.; Parish, C. A.; Pomerantz, A. E.; Mullins, O. C.; Zare, R. N. Nanoaggregates of Diverse Asphaltenes by Mass Spectrometry and Molecular Dynamics. *Energy Fuels* **2017**, *31* (9), 9140−9151.

https://dx.doi.org/10.1021/acs.energyfuels.0c00068
Energy Fuels 2020, 34, 4289−4295